Cd^{2+} incorporation in small-pore LEV/ERI intergrown zeolites: a multi-methodological study

Georgia Cametti*[a], Andreas C. Scheinost[b,c], Sergey V. Churakov[a,d]

[a] Institute of Geological Sciences, Baltzerstrasse 1+3, 3012 Bern, Switzerland

[b] The Rossendorf Beamline at the European Synchrotron Radiation Facility (ESRF), Avenue des Martyrs 71, 38043 Grenoble, France

[c] Helmholtz Zentrum Dresden Rossendorf, Institute of Resource Ecology, Bautzner Landstrasse 400, 01328 Dresden

[d] Paul Scherrer Institut, Forschungstrasse 111, 5232 Villingen PSI, Switzerland

Abstract

Small-pore zeolites are successfully employed as catalysts, sorbents and molecular sieves. Their physiochemical properties can be tuned by modifying their extraframework cation (EF) composition via ion exchange. In this study, we investigate the crystal structure of a Cd-exchanged levyne (**LEV**) intergrown with erionite (**ERI**) by combining Single Crystal X-ray Diffraction (SCXRD), Molecular Dynamic simulations (MD) and Extended X-ray Absorption Fine-Structure spectroscopy (EXAFS). Data obtained from the different techniques consistently indicate that Cd^{2+} in **LEV** is arranged in a nearly ordered fashion. In contrast, strong disorder of the EF species (Cd^{2+} and H_2O) is observed in the **ERI** cavities. Here, Cd^{2+} forms aqueous complexes that are more mobile in comparison to **LEV**, where Cd^{2+} bonds to both H_2O and framework-oxygen atoms. The formation of Cd-clusters is excluded based on EXAFS analysis. Finally, to discriminate between thermal and static disorder, we propose a new approach based on combined MD and geometry optimization.

Keywords: levyne, Cd-LEV, XRD, EXAFS, MD simulations, zeolites

*Corresponding author:

Georgia Cametti

Email: georgia.cametti@geo.unibe.ch

1. Introduction

Small-pore zeolites are crystalline materials with pore sizes between 0.30-0.45 nm [1]. The framework is mainly constituted by (SiO_4) and (AlO_4) tetrahedra. The latter build up pores with the maximum aperture-window constituted by eight-membered rings (8MR), which allow passage of only small molecules. In the past decades, research has been focussed on small-pore zeolites (compared to those with medium and large micropores) because of their advantageous use in catalytic processes such as exhaust cleaning, partial oxidation of methane and olefin generation [1].

Up to now, forty-four framework types (natural and synthetic) are classified as small-pore zeolites or 8MR zeolites. Among them, levyne (**LEV**) and erionite (**ERI**) are two naturally occurring zeolites belonging to the so-called ABC-6 family [2]. Levyne is described in the trigonal space group *R*-3*m* [2,3]. Single six-membered rings (6mR) of tetrahedra are stacked along the c-axis (stacking sequence AABCCABBC), forming the *lev* cavity (pore descriptor $4^9 6^5 8^3$) and the D6R cage consisting of double six-membered rings (pore descriptor $4^6 6^2$). Two interconnected 8-membered ring channels run parallel to [100]. The distribution of the extraframework (EF) cations differs from sample to sample, based on the chemical composition [4-7]. In general, the EF cations are located along the three-fold axis in the *lev* cavity whereas at room temperature (RT) no cations are found in the D6R cage. Similar to levyne, the erionite structure is constituted by 6mR of tetrahedra, but a different stacking sequence along the c-axis (AABAAC) creates a different system of channels and cavities. In erionite, the alternation of *eri* cavities [$4^{12}6^{5}8^{6}$] and cancrinite cages [$4^{6}6^{5}$] along c results in the hexagonal space group $P6_3/mmc$ [3,8]. Due to their structural similarity, these two zeolites are often found as intergrown phases in nature [9-12]. Concerning the synthesis route, **LEV** microporous aluminosilicates are always synthesized with the use of an overall structure-directing agent (OSDA) [1], whereas synthesis of pure **ERI** (with TMA) is difficult because it is often intergrown with offretite **(OFF)** [13]. In addition, a **LEV**/**ERI** intergrowth (SSZ-105) is also reported in the patent literature [14]. From an applicative point of view, levyne is mainly used for separation and sorption whereas the main exploitation of **ERI** materials is in catalysis [1 and reference herein].

Ion exchange is the most common method to change and tune the physio-chemical properties of zeolites. A large number of studies has been dedicated to the investigation of zeolites (natural and synthetic) exchanged with transition metals (Cu, Zn, Ag, etc.). Among them, Cd^{+2}-exchanged hydrated and dehydrated zeolite structures [15-20] were extensively investigated due to their attractive catalytic capacities [21-23]. Since the chemical reactivity depends on the type of cationic complexes, understanding the nature of the metal species (aquo complexes, charged clusters, etc.) and their interaction with the zeolitic framework is crucial to further tune and improve their applications. The exact determination of their coordination chemistry is, however, often compromised by high disorder of the EF species. In this case, the widely adopted X-ray based diffraction methods have to be accompanied by other techniques able to probe the short-range order of the species of interest. In particular, experimental and theoretical methods such as X-ray absorption spectroscopy (XAS) and molecular dynamics (MD) simulations have been successfully applied as complementary techniques to analyze the structure, oxidation state and bonding characteristics of metal species inside zeolites [24-27].

Recently, we characterized from a structural and chemical point of view an Ag^{+1}-exchanged levyne intergrown with erionite [28,29]. Our results show that Ag^{1+} replaces the original EF cations in both zeolites. In Ag-levyne, Ag ions were strongly disordered at partially occupied sites. Heating of this Ag-exchanged material induced a different dehydration path compared to the pristine material (i.e. levyne-Ca), even though the *R*-3*m* space group was maintained at RT. In the same study, we were able to characterize the intergrown Ag-erionite. Here, Ag^{+1} ions were located in the *eri* cavity, while the K atoms, originally in the cancrinite cage, could not be exchanged.

In this study, we report a detailed investigation of the structural incorporation of Cd^{2+} into levyne intergrown with erionite. The aim was to: i) determine the coordination chemistry and location of Cd^{2+} species in the two zeolites; ii) understand the effect of the framework type (**LEV** and **ERI**) on the Cd^{2+} distribution; iii) conceive a theoretical approach able to describe the disorder of the EF species. To reach these goals, experimental techniques were coupled with theoretical computations. Bulk structural data were obtained by Single Crystal X-Ray Diffraction (SCXRD) whereas X-ray Absorption Fine Structure (XAFS) spectroscopy and Molecular Dynamics (MD) simulations were used to get an insight into the local environment of Cd^{2+} and H_2O location within the zeolitic channels. This approach allowed us to obtain detailed information on the EF cation location and to compare the EF cation distribution with that of previously reported other cationic forms of levyne.

This kind of research is fundamental to exploit the potential application of the new porous phase. Several studies on metal-exchanged zeolites have demonstrated that even if the position of the EF cations has little influence on the RT structure, it plays a key role on the structural modifications occurring upon heating, leading to different dehydration paths and new porous phases.

2. Methods

2.1 Sample description

The pristine levyne sample was a levyne-Ca from Beech Creek, Oregon, U.S.A. (sample number A7827 of Natural History Museum of Bern) with chemical composition $Ca_{2.53}Na_{0.72}K_{0.23}(Al_{6.26}Si_{11.8}O_{36})\cdot 17.58\ H_2O$. The specimen was the same as used in our previous studies [28,30] and consisted of levyne intergrown with erionite [28]. For the diffraction experiments a single fragment of each phase could be separated whereas the XAFS measurements were performed on powder (see section 2.6) consisting of both levyne and erionite.

2.2 Exchange experiments

The exchange experiments were performed in two steps. First, small fragments (dimension between 100-400 μm) of natural levyne intergrown with erionite were put in an autoclave filled with 2M NaCl solution at 100°C for 4 weeks. The solution was renewed every three days. After that, the crystals were removed from the autoclave and washed with deionized water. This first step produced a partially exchanged Na-levyne, with residual Ca content non-homogeneously distributed in the crystals. Second, the partially Na-exchanged crystals were brought in contact with a 1 M $Cd(CH_3COO)_2$ solution (pH ≈ 6) for 4 weeks at 100°C. Similar to step 1, the solution was renewed every three days. After the exchange experiments the crystals were washed with deionized water and the chemical composition was controlled by energy dispersive spectrometry (EDS) using a ZEISS EVO50 scanning electron microscope (SEM).

2.3 Chemical analyses

To determine the effect of the exchange process on both phases (i.e. levyne and erionite), chemical analyses were performed on different crystal fragments. The two zeolites could be distinguished based on their different crystal morphology, i.e. bulky for levyne and fibrous for erionite [28] (see results section). Operating conditions for EDS were 20 kV, accelerating voltage, 10 mm working distance, 30 s acquisition time. The chemical formula was calculated based on 36 (Si+Al) atoms after renormalization of the chemical analyses assuming a water content of 18% wt. The reliability of the chemical analyses was evaluated by the charge balance error test [31].

2.4 Single Crystal X-ray Diffraction (SCXRD)

A single fragment of Cd-levyne with dimension 0.10 x 0.12 x 0.13 mm was glued on the tip of a glass fibre mounted on a goniometer head. Diffraction data were collected using a Synergy-S Rigaku diffractometer equipped with a dual micro-focused source and a Hypix detector. AgKα radiation (λ = 0.56087 Å) was chosen to minimize the absorption of cadmium. Data were integrated and corrected for absorption with the CrysAlisPro 171.40.29a software package [32]. Structure solution by direct methods using Shelxt [33] indicated space group *R*-3*m*.

To determine the structure of the intergrown erionite, a smaller fragment (0.01 x 0.07 x 0.08 mm) was selected under a binocular microscope, glued on the tip of a glass fibre and mounted on a goniometer head. Due to the small size of the crystal, diffraction data were collected using the more brilliant CuKα (λ = 1.54184 Å) radiation available on the same diffractometer utilized for

Cd-levyne. The data were reduced and corrected for absorption as before. The structure was solved by direct methods [33] in space group $P6_3/mmc$.

Structural refinements were carried out by using neutral atomic scattering factors by Shelxl [34]. Atomic labels and coordinates of the framework are as reported in Cametti and Churakov, 2020 [28]. EF cations and H_2O molecules were located by difference Fourier maps and labelled according to the nomenclature used for levyne-Ca [30].

Crystal data and refinements parameters are reported in Table 1. All structural drawings were produced with the VESTA software [35].

2.5 Molecular dynamics (MD) simulations

The MD simulations were run using the Cp2k software package [36]. The calculations were performed in NPT (constant temperature and pressure, and flexible unit cell) ensemble based on Density Functional Theory (DFT). The integration time of the equations of motion was 0.5 fs. The simulation temperature of MD was set to 350 K to prevent the glassy behaviour of PBE-H_2O [37]. The electron exchange and correlations were described by the Perdew-Burke-Erzerhof functional [38]. The Kohn-Sham orbitals were expanded using a linear combination of atom-centred Gaussian-type orbital functions. A short-range double-ζ valence polarized basis set was employed for each atom kind [39]. Dispersion correction was taken into account using the DFT+2D method [40].

System set up. The starting coordinates of the Cd-LEV structural model were taken from X-ray data. The EF cations were considered to be solely Cd, located at the most occupied sites as retrieved from X-ray structural refinement. The number of H_2O molecules was set according to the chemical composition, i.e. 6 H_2O per Cd^{2+} ion. A fully flexible supercell 2 × 1 × 1, containing

18 Cd, 72 Si, 36 Al, 323 O, and 216 H was used. The structure of Cd-erionite was simulated using a flexible supercell 1 × 1 × 1.5 containing 6 Cd, 3 K, 39 Si, 15 Al, 109 O, and 37 H_2O. Starting coordinates were taken from X-ray data.

For both structures, data were collected from a 15 ps long trajectory followed by at least 6 ps pre-equilibration. Theoretical Cd K-edge Extended X-ray Absorption Fine Structure (EXAFS) spectra were calculated for each Cd^{2+} position in the supercell using the FEFF 8.40 software [41,42]. The Fermi energies and the scattering potential were modelled self-consistently using a cluster radius of 4 Å. Because the structural disorder is taken into account in MD trajectories, the Debye-Waller factor was set to 0.0002 $Å^2$. The amplitude reduction factor (S_0) was set to 0.9. For Cd-levyne, 136 consequent frames separated by 125 fs interval were used to calculate an average EXAFS spectrum. Similarly, 136 consequent snapshots separated by 100 fs interval were used to calculate the EXAFS spectrum of Cd-erionite.

To discriminate between the effect of vibrational (the MD simulations were run at 350 K) and that of static disorder on the EXAFS spectra, a sequence of geometry optimizations was run for each phase (Cd-LEV and Cd-ERI) using the following method: 1) the atomic coordinates and unit cell parameters were taken from 10 subsequent MD snapshots, in the range from 10 to 20 ps in steps of 1 ps; 2) geometry and cell optimization were run for each snapshot; 3) for each optimized structure (ten in total for Cd-LEV and Cd-ERI), a theoretical EXAFS spectrum was obtained by averaging the spectra calculated for each Cd^{2+} in the supercell. The Debye-Waller factor in this case was set to 0.002 $Å^2$. Finally, an average EXAFS spectrum was obtained for both Cd-LEV and Cd-ERI by averaging the ten spectra calculated in step 3.

2.6 Extended X-ray Absorption Fine Structure Spectroscopy (EXAFS)

EXAFS data were collected at the Rossendorf Beamline [43] at the European Synchrotron Radiation Facility (ESRF) in Grenoble (France) using a Si(111) double-crystal monochromator and two Pt-coated mirrors for collimation and suppression of higher-order harmonics. The sample was gently ground, homogeneously mixed with boron nitride and subsequently pressed to form a pellet, which was covered with Kapton tape and inserted in a sample holder. The sample was measured in transmission mode under cryogenic conditions (~15 K) to supress thermal contributions to the Debye-Waller term, using Ar-filled ionization chambers. Five individual XAS scans were energy-calibrated against a simultaneously measured Cd foil (26711 eV) and averaged using SIXpack, while subsequent data reduction steps and shell fits were conducted using WinXAS [44,45].

EXAFS analysis was performed by Fourier transforming the k^3- weighted $\chi(k)$- function between 2 and 14.5 Å^{-1} using a Kaiser-Bessel window function. Theoretical backscattering paths were calculated with FEFF8.2 [41,42] using the Cd-levyne structure model used for DFT calculations. The refinement was carried out in Fourier space by a multishell fit approach. The amplitude factor S_0 was set to 0.9 and a global phase shift ΔE was fitted for all paths.

3. Results

The investigated sample is characterized by two intergrown mineral phases with two different chemical compositions: one with a bulky morphology, corresponding to levyne and the other with a fibrous-like morphology identified as erionite (Figure S1). The EDS-SEM analyses of the levyne fragments indicated that Na was completely replaced by Cd during the two-step ion exchange procedure. However, residual Ca (varying from 0.39 to 0.7 apfu) was detected at all analysed points. In contrast, the erionite fragments contained only K and Cd as extraframework cations

(EF). The final chemical composition was $Cd_{2.6}Ca_{0.6}Al_{6.6}Si_{11.4}O_{36}\cdot 18.0H_2O$ and $Cd_{2.2}K_{1.2}Al_{5.6}Si_{12.4}O_{36}\cdot 18H_2O$ for Cd-levyne and –erionite, respectively.

3.1 Crystal structure of Cd-levyne. The structure maintained the *R*-3*m* space group characteristic of the natural levyne-Ca and of the Ag-exchanged one [28,30]. The unit cell volume was smaller, however, as expected by the smaller radius of Cd^{2+} compared to that of Ag^{1+} and Ca^{2+}.

According to the structural refinement (Table 2), Cd ions are predominantly residing at C1 (Occ. = 0.778(6)) and C5 (Occ. = 0.469(8)) sites. The C3 site, refined with Ca scattering factors, is 50% occupied (Fig. 1a,b). The H_2O molecules are located at four sites corresponding to W1, W2, W3, and W4 of the natural levyne-Ca.

C1 is coordinated by three H_2O at W1 (d = 2.329(7) Å) and by three framework-oxygen atoms at O2 (d = 2.374(5) Å), whereas C5 is at the top of the *lev* cavity and bonds to six framework oxygen atoms at O5 (d =2.556(6) Å). C3 bonds to three H_2O at W2 (2.764(16) Å) and to three H_2O at W3 (2.21(5) Å). Such short Ca-O distances suggest a partial occurrence of Cd^{2+} ions at this site, further corroborated by the slightly higher Ca amount (1 apfu), obtained by the structural refinement, compared to that determined by the chemical analyses (0.6 apfu).

The structural parameters extrapolated form MD trajectories are consistent with those obtained by XRD, indicating that the residual amount of Ca in the *lev* cavity has overall a negligible effect. In the theoretical structure, assuming only Cd^{+2} EF cations, Cd mainly locates at the top and bottom of the *lev* cavity (Fig. 2a), corresponding to the C1 and C5 sites. The local coordination environment of Cd^{2+} ions, which mainly bond to H_2O and framework oxygen of the D6R cage, also agrees with that determined by diffraction data (Fig. 2b). The analysis of the Cd-O bonds is reported in Fig. 2c. The radial distribution function (RDF) and corresponding coordination number (CN) were calculated for Cd-O (O oxygen of the framework) and Cd-Ow (Ow water molecules) pairs. The Cd-Ow curve has a maximum at 2.28 Å, whereas the Cd-O curve appears broader, with Cd-O distances mainly distributed between 2.32 and 2.43 Å. On average, each Cd is surrounded by two-framework oxygen atoms and by three H_2O with distances between 2.2 and 2.5 Å.

3.2 Crystal structure of Cd-erionite. The structural parameters of Cd-erionite and corresponding relevant bond distances are reported in Table 3 and 4, respectively. The space group $P6_3/mmc$ is identical to that of natural erionite [8].

In agreement with previous findings [46], the exchange process had no effect on the original K atoms, which remained in the cancrinite cage. Cadmium is found in the *eri* cavity, disordered at partially occupied sites. These positions are somewhat similar to those of the EF cations observed in Ag-exchanged erionite [28]. In particular, C1, C2 and C3 correspond to the sites with equivalent label in the structure of Ag-erionite. C1 (split in two subsites, C1 and C1A) is close to the wall of the six-membered ring window of the cancrinite cage. C2 (the most occupied site) and C2A are in the centre of the 6mR, at the top and bottom of the *eri* cavity. C3 is in the middle of the cavity, surrounded by two additional sites C4 and C4A (site symmetry 24l), which distribute in a ring-like fashion, above and below C3 (Fig. 3). C4, C4A and C3 have a low occupancy (<0.10) and are close to each other (distances 1.5-2-13), indicating pronounced disorder of Cd^{2+} in the erionite cavity. The H_2O molecules are also disordered at partially occupied sites, mainly in the 8mR window of the *eri* cavity and along the sixfold inversion-axis, bonded to C2. The strong disorder of the EF species may also justify the lack of approximately 25% of Cd atoms that could not be located by the structural refinement.

Such disordered configuration complicated the interpretation of the coordination of Cd in erionite. In this specific case, we relied on the MD simulations. A snapshot of the arrangement of Cd and

H_2O in the calculated structure is showed in Fig. 4a. In agreement with XRD, the MD trajectories showed that Cd adopted diverse positions in each cavity. Cd ions in the centre of the *eri* cavity are displaced off the sixfold inversion-axis, toward the wall of the cavity. In addition, Cd at the bottom and top of the cavity (C2, C2A sites in XRD refinement) are off from the centre of the 6mR.

The distribution of Cd-O distances (Fig. 4b) is similar to that obtained for Cd-levyne. Cd mainly bonds to H_2O, with about 2 Ow between 2.27 and 2.32 Å, whereas the Cd-O distances extend across a very broad range, with a maximum at 2.43 Å, where approximately one framework oxygen atom only is found.

3.3 Local environment of Cd^{2+}

The experimental, k^3-weighted Cd K-edge EXAFS function and corresponding FT (uncorrected for phase shift) are reported in Fig. 5a,b. Note that the spectrum contains the proportional Cd contributions of both Cd-LEV and –ERI. The first peak at 1.8 Å was fitted by one Cd-O shell with Cd-O distance of R = 2.29 Å and CN = 6. To properly fit the second peak at 1.9 Å different tests were performed using a single shell (Cd-Si or Cd-Ca) or a double-shell scheme (Cd-Si, Cd-Si or Cd-Si, Cd-Ca). The best fit was obtained with two Cd-Si shells at R = 3.15 Å and R = 3.44 Å (Table 5). Furthermore, an attempt was made to fit the small peak at 4.49 Å in the FT (Fig. 5b). According to XRD data, such broad peak at that distance is in agreement with the presence of K in the Cd-ERI phase. Nevertheless, a tentative fitting including an additional Cd-K scattering path was not successful and was hence not further considered.

The Cd-O distances obtained by EXAFS analysis agree with those extrapolated by SCXRD refinement and MD trajectories. The most occupied EF sites in Cd-levyne and Cd-erionite are C1 and C2, respectively. C1 in Cd-LEV bonds to W1 at 2.329(7) Å and C2 in Cd-ERI to W5 at 2.27(3)

Å. Such distances are also in agreement with those reported by the MD trajectories, which indicated that, for both phases, the main peak of Cd-H_2O interactions is at 2.28 Å. The distances of the Cd-Si shell (Table 5) also match those of the simulated (Fig. 6) and refined structures. In Cd-LEV, similar distances are found between C5 and T2 sites (3.1781(17) Å) and C1 and T1 sites (3.4618(12) Å). Similarly, C2-T2 sites in Cd-ERI are at 3.216(1) Å.

4. Discussion

4.1 Static disorder and thermal motion

To try to unravel the contribution of each phase to the EXAFS spectrum, theoretical k^3-weighted chi functions were calculated based on the MD trajectories for both Cd-LEV and Cd-ERI. Fig. 7a reports the experimental and the average theoretical chi function using a levyne/erionite ratio of 45:55. Such ratio, instead of 50:50 as reported in [29], was used to take into account the slight overestimation of Cd content in the simulated Cd-LEV structure (9 Cd vs 7.8 pfu calculated from chemical analysis). The theoretical spectra obtained from MD trajectories at ambient conditions (of both Cd-LEV and Cd-ERI (Fig. S2)), substantially underestimate the intensities of the experimental κ^3-$\chi(\kappa)$ functions collected at 15 K (Fig. 7a). Two factors influence the amplitude of the EXAFS- k^3-weighted $\chi(\kappa)$ function: i) the coordination number (positive correlation) and ii) the Debye-Waller factor (negative correlation). Since the structural models obtained from EXAFS shell fitting and from MD are in good agreement, and since the effect is more pronounced at high k values, it could be inferred that the mismatch of intensities results from the thermal contribution to the Debye-Waller factor; note that the experimental spectra have been collected at 15 K, where thermal disorder is negligible, while the MD calculation were performed at 350 K, where thermal contribution may dominate the Debye-Waller term. To mimic the low temperature conditions (low thermal disorder) and at the same time to account for the structural disorder, a set of geometry optimisations was performed starting from the uncorrelated atomic configuration collected from MD simulations at 350 K (as described in section 2.5).

By doing so, we expect to obtain a number of structural configurations with atoms confined to the local energy minima but representing structural disorder as it would be obtained for the geometry optimization in a very large supercell. In this approach, the MD trajectory is used to collect the thermally disordered structure, whereas geometry and cell optimisation bring the atoms towards the nearest local minima as expected to occur during the experimental measurement.

Theoretical EXAFS spectra were then calculated for this set of geometry and cell optimised configurations. The such-obtained EXAFS spectra show a much better agreement with the experimental data, though a partial mismatch between the amplitudes is still visible (Fig. 7b). A slight shift toward lower κ values is also observed. An inspection of the κ^3-$\chi(\kappa)$ function of the single components (Cd-LEV and Cd-ERI) indicated that such shift is mainly caused by the Cd-LEV phase (green curve in Fig.S3). These discrepancies might be related to the presence of residual Ca or a slightly different hydration shell [47].

4.2 Influence of the framework type on the disorder of the EF species

The results obtained by the different techniques consistently show that in Cd-LEV, Cd^{+2} ions distribute in a fairly ordered fashion within the pores. In particular, they mainly replace the cations at the most occupied crystallographic sites (i.e. C1, C3, and C5) present in levyne-Ca. In contrast, in Cd-ERI, the disorder is much more pronounced, and no obvious parallelism can be drawn with the EF site positions of natural erionite [8]. The arrangement of cadmium in the erionite pores resembles that of silver in Ag-exchanged erionite [28], though strong differences appear in site occupancy. For example, the C1 site (occ. = 0.70), where most of Ag^{+1} ions are located in the Ag-

ERI structure, is much less occupied in Cd-ERI (occ. = 0.20). The Cd ions are significantly more diffuse in erionite than in levyne, especially if the centre of the *eri* cavity is considered. Interestingly, the opposite situation is found in the Ag-exchanged forms, where Ag ions are more diffuse and disordered in levyne compared to erionite [28]. It was suggested that the coordination chemistry of EF species in hydrated zeolites is close to that in aqueous solutions [48]. Hence the exchanged cations are in form of “aquo complexes that are mobile and only partially coordinated to framework oxygen in a dynamically disordered fashion” [48]. The same authors also pointed out that “the steric constraints imposed by” smaller pores “promote greater ligand dissociation during cation exchange” [48], which induces a greater interaction with the framework oxygen. Although the aperture diameters and hence the access to the respective zeolitic cavities is the same in **LEV** and **ERI** (i.e. 8MR), the *eri* cavity is significantly bigger than the *lev* one. Thus, the higher mobility of the most hydrated Cd ions in the *eri* cavity could be one cause of the greater disorder observed in Cd-ERI. The analysis of the Cd-OW distal distribution (Fig.2c and 4b) in Cd-LEV and Cd-ERI confirms that Cd^{2+} is “more hydrated” in erionite than in levyne, supporting our hypothesis. In levyne, Cd^{2+} coordinates to H_2O and framework oxygen, and $Cd^{+2}(H_2O)_6$ complexes do not form. In Cd-ERI, Cd ions in the middle of the *eri* cavity can be fully hydrated (and hence more mobile) (Fig.8a) or partially coordinated by framework oxygen atoms (Fig.8b).

4.3 Cationic cluster formation

The formation of cationic Cd_n^{m+} clusters in zeolites was first concluded from Raman measurements [49] and reported for zeolite A [15,20,50]. Although in the structure of erionite the arrangement of C3 and C4 (Cd-Cd = 2.6 Å) resembles that of a cluster Cd_9^{8+} reported in the sodalite cage of zeolite A [20], we can exclude the formation of metallic Cd based on our EXAFS analysis: neither did we observe the characteristic X-ray absorption near-edge structure (XANES) of Cd^0, easily distinguishable from the observed XANES of Cd^{+2} (Fig. S4), nor could we identify with wavelet analysis [51] a Cd-Cd backscattering contribution to the FT peak at about 3 Å, indicative of clusters of metallic Cd (Fig. 5). Furthermore, our sample was measured at 15 K without previous dehydration by thermal and/or vacuum treatment, whereas Cd clusters reported in zeolite A were observed only in dehydrated samples. Thus, it can be hypothesized that the hydration shell of Cd ions in both zeolites (Cd-LEV and Cd-ERI) prevents Cd clustering.

5. Conclusions

The investigation of EF species in zeolites can be challenging when both H_2O and charge-compensating cations are disorderly distributed in the pores. Although X-ray diffraction is one of the most used technique, additional methods are needed to properly characterize the position and coordination chemistry of the EF cations. In our study, we used a complementary experimental and theoretical approach to investigate in detail the Cd^{2+} arrangement in small-pore zeolites, **LEV** and **ERI**. We found that, although the local environment of Cd^{2+} is similar in the two zeolites, differences in terms of disorder and coordination shell arise because of the different framework types (i.e. kind of cavities). Cd ions are octahedrally coordinated by H_2O and framework oxygen in **LEV**, and are in the *lev* cavity arranged in an almost ordered manner. In Cd-ERI, more mobile $Cd(H_2O)_6$ complexes are present in the middle of the *eri* cavity (even though Cd^{2+} partially coordinates to framework oxygen atoms), leading to significant positional and dynamical disorder. High quality experimental EXAFS spectra and the molecular simulations allowed us to discriminate for the first time the effect of thermal and structural disorder in the measured and theoretically calculated EXAFS spectra based on the MD trajectories and structural geometry optimisation.

Acknowledgements

We are thankful to Dr. Beda Hoffman of the Natural History Museum of Bern who provided the levyne sample and to Thomas Armbruster who read the manuscript. We acknowledge access to the Swiss National Supercomputing Center (CSCS) and the UBELIX HPC cluster at the University of Bern.

Funding

The Swiss National Science Foundation (SNF) is acknowledged for the Ambizione grant n. PZ00P2 173997 awarded to G. C. and for the R'Equip grant n. 206021_177033 awarded to P. Macchi.

References

[1] M. Dusselier, M. E. Davis, Chem. Rev. 118 (2018) 5265-5329.
[2] R. M. Barrer, I.S. Kerrer, Trans. Faraday Soc. 55 (1959) 1915-1923.
[3] G. Gottardi, E. Galli, Natural Zeolites, vol. 18 Springer-Verlag, Berlin, 1985409.
[4] S. Merlino, E. Galli, A. Alberti, Tscher. Miner. Petrog. 22 (1975) 117-129.
[5] M. Sacerdoti, Jb Neues Miner. Monat. 3 (1996) 114-124.
[6] G. D. Gatta, P. Comodi, P. Zanazzi, T. Boffa Ballaran, Am. Mineral. 90 (2005) 645-652.
[7] P. Ballirano, G. Cametti, Mineral. Mag. 77 (7) (2013) 2887-2899.
[8] A. Alberti, A. Martucci, E. Galli, G. Vezzalini, Zeolites 19 (1997) 349-352.
[9] M. Shimazu, T. Mizota, J. Jap. Ass. Mineral. Petr. Econ. Geo. 67 (1972) 418-424.
[10] J. M. Bennett, R. W. Grose, (1978) In: Sand L. B., Mumpton, F. A., (eds) Natural Zeolites. Pergamon, Oxford, pp 77-84.
[11] S. W. Wise, R. W. Tschernich, Am. Mineral. 61 (1976) 853-863.
[12] E. Passaglia, E. Galli, R. Rinaldi, Contrib. Mineral. Petr. 43 (1974) 253-259.
[13] K. P. Lillerud, J. H. Raeder Zeolites 6 (1986) 474-483.
[14] D. Xie, Lew C. M. US Patent 9663380 2017.
[15] L. B. McCusker, K. Seff, J. Am. Chem. Soc. 101 (1979), 5235– 5239
[16] S. B. Jang, U. S. Kim, Y. Kim, K. Seff, J. Phys. Chem. 98 (1994) 3796-3800.

[17] Y. Lee, B. A. Reisner, J. C. Hanson, G. A. Jones, J. B. Parise, D. R. Corbin, B. H. Toby, A. Freitag, J. Z. Larese, J. Phys. Chem B 105 (2001) 7188-7199.

[18] E. Y. Choi, S. H. Lee, Y. Kim, Y. W. Han, K. Seff, J. Phys. Chem. B 106 (2002) 7569–7573.

[19] J. Wang, D. Wang, H. Zeng, Z. Zhou, RSC Advances 5 (2015) 77490-77494

[20] J. E. Readman, P. D. Barker, I. Gameson, J. A. Hriljac, W. Zhou, P.P. Edwards, P. Anderson, Chem. Commun. (2004) 736-737.

[21] G. Onyestyak, D. Kallo, Microporous Mesoporous Mater. 61 (2003) 199-204.

[22] Y. Zhang, Y. Qu, D. Wang, X. C. Zeng, J. Wang, Ind. Eng. Chem. Res. 56 (2017) 12508-12519.

[23] P. Aprea, B. De Gennaro, N. Gargiuolo, A. Peluso, B. Liguori, F. Iucolano, D. Caputo, Appl. Therm. Eng. 106 (2016) 1217-1224.

[24] V. V. Speybroeck, K. Hemelsoet, L. Joos, M. Waroquier, R. G. Bell, C. R. A. Catlow, Chem. Soc. Rev. 44 (2015) 7044-7111.

[25] E. Borfecchia, K. A. Lomachenko, F. Giordanino, H. Falsig, P. Beato, A. V. Soldatov, S. Bordiga, C. Lamberti, Chem. Sci. 6 (2015) 548-563.

[26] I. A. Pankin, A. Martini, K. A. Lomachenko, A. V. Soldatov, S. Bordiga, E. Borfecchia, Catalysis Today, 345 (2020) 125-135.

[27] G. Beltrami, T. Chenet, L. Pasti, L. Gigli, S. Pollastri, A. Martucci, Catalysis Today, 345 (2020) 147-156.

[28] G. Cametti, S. V. Churakov, Am. Mineral. 105 (2020) 1631-1638.

[29] G. Cametti, A. C. Scheinost, S. V. Churakov ACS Omega, http://dx.doi.org/10.1021/acsomega.0c04455.

[30] G. Cametti, Microporous Mesoporous Mater. 265 (2018) 162-171.

[31] E. Passaglia, Am. Mineral. 55 (1970) 1278-1301.

[32] CrysAlisPro, Rigaku Oxford diffraction, 2018, Version 171.40.29a.

[33] G. M. Sheldrick, Acta Crystallogr. A 64 (2008) 112-122.

[34] G. M. Sheldrick, Acta Crystallogr. C 71 (2015) 3-8.

[35] K. Momma, F. Izumi, J. Appl. Crystallogr. 44 (2011) 1272-1276.

[36] T. Kühne, M. Iannuzzi, M. Del Ben, V. Rybkin, P. Seewald, et al. J. Chem. Phys. 152 (2020) 194103.

[37] J. Schmidt, J. VandeVondele, I. F. W. Kuo, D. Sebastiani, J. I. Siepmann, J. Hutter, C. J. Mundy, J. Phys. Chem. B 113 (2009) 11959-11964.

[38] J. P. Perdew, K. Burke, M. Ernzerhof, Phys. Rev. Lett. 77 (1996) 3865-3868.

[39] J. VandeVondele, J. Hutter, *J. Chem. Phys.* 127 (2007) 114105.

[40] S. Grimme, J. Comput. Chem. 27 (2006) 1787-1799.

[41] A. L. Ankudinov, B. Ravel, J.J. Rehr, S. D. Conradson, Phys. Rev. B 58 (1998) 7565-7576.

[42] A. L. Ankudinov, J. J. Rehr, Phys. Rev. B 62 (2000) 2437-2445.

[43] A. C. Scheinost, J. Claussner, J. Exner, M. Feig, S. Findeisen, C. Hennig, K. O. Kvashnina, D. Naudet, D. Prieur, A. Rossberg, M. Schmidt, C. Qiu, P. Colomp, C. Cohen, E. Dettona, V. Dyadkin, T. Stumpf, J. Synchrotron Rad. 28 (2021) 1.

[44] S. M. Webb, Physica Scripta **T115** (2005) 1011-1014.

[45] T. Ressler, J. Synchrotron Radiation 5 (1998) 118-122.

[46] H. S. Sherry, Clay Clay Miner. 27 (1979) 231-237.

[47] G. Cametti, A. C. Scheinost, S. V. Churakov J. Phys. Chem. C 123 (2019) 25236-25245.

[48] T. I. Morison, L. E. Iton, G. K. Shenoy, G. D. Stucky, S. L. Suib, J. Chem. Phys. 75 (1981) 4086-4089.

[49] A. Goldbach, P. D. Barker, P. A. Anderson, P. P. Edwards, Chemical Physics Letters 292 (1998) 137-142.

[50] S. B. Jang, U. S. Kim, Y. Kim, K. Seff, J. Phys. Chem. 98 (1994) 3796-3800.

[51] H. Funke, A. C. Scheinost, M. Chukalina Phys. Rev. B 71 (2005) 094110.

Tables

Table 1 Crystal data and refinement parameters of Cd-LEV and Cd–ERI.

Crystal data	**Cd-LEV**	**Cd-ERI**
a (Å)	13.3986(6)	13.2607(2)
c (Å)	22.3458(9)	15.2028(3)
V (Å^3)	3474.1(3)	2315.19(9)
Z	3	2
Space Group	*R*-3*m*	*P*6$_3$*/mmc*
Refined Chemical formula	$Cd_{2.03}Ca1(Si, Al)_{18}O_{36}\cdot14.16\ H_2O$	$Cd_{1.51}K(Si, Al)_{18}O_{36}\cdot13.8\ H_2O$
Crystal size (mm)	0.10 × 0.12 × 0.13	0.01 × 0.07 × 0.08
Intensity measurement		
Diffractometer	Rigaku Synergy-S	Rigaku Synergy-S
X-ray radiation	Ag*Kα* λ = 0.56087 Å	Cu*Kα* λ = 1.54184 Å
X-ray power	65 kV, 0.67 mA	50 kV, 1mA
Monochromator	Mirror Optics	Mirror Optics
Temperature (°C)	25	25
Exposure time (s)	115.1	0.54(min) -134(max)
Max. 2θ (°)	50.68	80.03
Index ranges	$-15 \leq h \leq 15$ $-16 \leq k \leq 17$ $-30 \leq l \leq 30$	$-16 \leq h \leq 12$ $-15 \leq k \leq 16$ $-14 \leq l \leq 18$
No. of measured reflections	7524	15565
No. of unique reflections	1237	989
No. of observed reflections I > 2σ (I)	1126	933
Structure refinement		
No. of parameters used in the refinement	76	101
R(int)	0.0497	0.0546
R(σ)	0.0253	0.0226
GooF	1.229	1.119
*R*1, *I*>2σ (*I*)	0.0562	0.0583
*R*1, all data	0.0602	0.0606
*wR*2 (on *F*^{2})	0.1928	0.1776

$\Delta\rho_{min}$ (-eÅ^{-3}) close to	-1.04 C3	-0.54 W2A
$\Delta\rho_{max}$ (eÅ^{-3}) close to	1.24 C3	1.73 K
BASF	0.029(4)	-

Table 2 Atom coordinates, occupancy and atomic displacement parameters of Cd-LEV

Site	Scattering factors	x	y	z	Occ.	U^{eq}
T1	Si	0.43834(10)	0.10490(10)	0.40498(5)	1	0.0211(4)
T2	Si	0.23720(12)	0	0.5	1	0.0192(4)
O1	O	0.3167(3)	0.0250(3)	0.44080(17)	1	0.0388(9)
O2	O	0.4941(5)	0.2471(2)	0.4203(2)	1	0.0331(11)
O3	O	0.5365(2)	0.0731(5)	0.4283(2)	1	0.0320(10)
O4	O	0.4128(4)	0.0794(4)	0.3333	1	0.0355(11)
O5	O	0.1091(3)	-0.1091(3)	0.4845(2)	1	0.0393(12)
C1	Cd	0.6667	0.3333	0.47742(5)	0.778(6)	0.0303(4)
C3	Ca	0	0	0.3945(13)	0.49(3)	0.177(13)
C5	Cd	0	0	0.5	0.469(8)	0.0281(9)
W1	O	0.8154(6)	0.4077(3)	0.5474(4)	1	0.074(3)
W2	O	0.0793(13)	-0.1527(12)	0.3769(6)	0.317(17)	0.053(5)
W3	O	0.412(2)	-0.176(4)	0.328(2)	0.25(3)	0.10(2)
W4	O	0.229(2)	-0.229(2)	0.351(2)	0.47(3)	0.2

Table 3 Relevant bond distances (Å) of the Cd-LEV structure at room temperature.

Framework			
T1-O4	1.6372(17)	T2-O1	1.625(3)
T1-O1	1.642(4)	T2-O1	1.625(4)
T1-O3	1.657(2)	T2-O5	1.6410(17)
T1-O2	1.697(3)	T2-O5	1.6411(17)
<T1-O>	1.658	<T2-O>	1.633
Extraframework			
C1-W1 x3	2.329(7)		
C1-O2 x3	2.374(5)		

C5-O5 x5	2.556(6)
C3-W3 x3	2.21(5)
C3-W2 x3	2.764(16)

Table 4 Atom coordinates, occupancy and atomic displacement parameters of Cd-ERI

Site	Scattering factors	x	y	z	Occ.	U^{eq}
T1	Si	0.23490(7)	-0.00024(7)	0.10353(6)	1	0.0248(4)
T2	Si	0.09172(10)	0.42327(10)	0.25	1	0.0223(4)
O1	O	0.09951(19)	0.1990(4)	0.1257(3)	1	0.0417(9)
O2	O	0.2693(4)	0	0	1	0.0416(10)
O3	O	0.0865(6)	0.5433(3)	0.25	1	0.0449(14)
O4	O	0.0243(3)	0.3508(3)	0.16049(19)	1	0.0451(7)
O5	O	0.2288(3)	0.4577(5)	0.25	1	0.0459(14)
O6	O	0.2528(4)	0.12640(19)	0.1332(3)	1	0.0434(10)
K	K	0	0	0.25	1	0.0399(7)
C1	Cd	0.3961(4)	0.19807(19)	0.25	0.137(3)	0.0380(16)
C1A	Cd	0.483(3)	0.2415(13)	0.25	0.072(7)	0.18(2)
C2	Cd	0.3333	0.6667	0.25	0.28(2)	0.0252(19)
C2A	Cd	0.3333	0.6667	0.276(2)	0.066(12)	0.025(5)
C3	Cd	-0.3333	0.3333	0.2149(13)	0.053(4)	0.069(7)
C4	Cd	0.527(5)	0.263(3)	0.352(4)	0.018(2)	0.1*
C4A	Cd	0.548(2)	0.359(3)	0.3488(19)	0.0229(14)	0.1*
W2	O	0.0258(16)	0.5129(8)	0.0828(6)	0.48(5)	0.017(3)
W2A	O	-0.0077(17)	0.4961(9)	0.0939(7)	0.45(4)	0.012(3)
W2B	O	0	0.5	0	0.18(3)	0.1*
W4	O	-0.1068(19)	0.4466(10)	0.1434(16)	0.27(3)	0.035(5)
W4A	O	-0.074(2)	0.4630(10)	0.1158(14)	0.25(3)	0.021(5)
W4B	O	0.115(3)	0.5575(15)	0.015(2)	0.59(4)	0.23(2)
W5	O	0.3333	0.6667	0.400(2)	0.51(4)	0.108(13)

*fixed

Table 5 Relevant bond distances (Å) of Cd-ERI structure at room temperature.

Framework			
T1-O6	1.6375(14)	T2-O3	1.6267(11)
T1-O2	1.6383(16)	T2-O5	1.6385(18)
T1-O1	1.6452(15)	T2-O4	1.648(3)
T1-O4	1.647(3)	T2-O4	1.648(3)
<T-O>	1.642	<T-O>	1.640
Extraframework			
K1-O1 ×6	2.966(4)		
C1-O6 ×2	2.421(5)		
C2-W5 ×2	2.27(3)		
C2-O5 ×2	2.400(6)		
C2A-O5 ×2	2.431(8)		
C4-W4 ×2	2.274(19)		
C4-W2A	2.34(4)		

Table 6 Structural parameters of Cd-LEV-ERI at 15 K determined from EXAFS analysis

Shell	**CN** ±25%	**R(Å)** ±0.02	**σ^2 (Å^2)** ±0.002
Cd-O	6.14	2.29	0.006
Cd-Si	1.11	3.15	0.008*
Cd-Si	4.06	3.44	0.008*
ΔE_0(eV)		9.06	
χ-residual		4.73	

*constrained to be equal

CN: Coordination Number

R: Absorber-scatterer distance

σ^2: Debye-Waller factor

Figures Caption

Figure 1 Crystal structure of Cd-LEV determined by SCXRD projected along [210] (a) and [100] (b). Oxygen and Si atoms are shown as blue and red spheres, respectively. Fuchsia and dark cyan spheres represent Cd and Ca, respectively. Partially coloured balls represent partial occupancy of atom sites. The atomic labels of the extraframework cations and water molecules are reported.

Figure 2 Snapshot of the simulated structure of Cd-LEV at 23 ps (a). Colour code as in Figure 1. Al atoms and hydrogen are shown in light blue and pink, respectively. (b) Detail of the coordination of the Cd atoms to the 6DR cage of Cd-LEV. (c) Radial distribution function (RDF) (continuous lines) and coordination number (CN) (dotted lines) of Cd-O (O = framework oxygen) and Cd-Ow (Ow = water molecules) contacts in Cd-LEV obtained from MD trajectories. Blue dotted lines are guidelines.

Figure 3 Crystal structure of Cd-ERI obtained from SCXRD. Colour code as in Figure 1. K atoms are shown in purple.

Figure 4 (a) Snapshot of the simulated structure of Cd-ERI at 22 ps. Colour code as in Figure 2. Green dotted lines indicate the sixfold inversion-axis (b) Radial distribution function (continuous lines) and coordination number (dotted lines) of Cd-O (O = framework oxygen) and Cd-Ow (OW = water molecules) distances in Cd-ERI obtained from MD trajectories.

Figure 5 Cd K-edge EXAFS spectra of Cd-LEV-ERI measured at 15 K, showing (a) the κ^3-weighted $\chi(\kappa)$ function and (b) the Fourier transform (uncorrected for phase shift). Blue circles and red lines represent the experimental Fourier transform magnitude and its corresponding fit, respectively. Experimental (dashed line) and fitted (continuous line) imaginary parts of the FT are also shown**.**

Figure 6 Radial distribution function (continuous lines) and coordination number (dotted lines) of Cd-Si and Cd-Al distances in Cd-LEV (a) and Cd-ERI (b) obtained from MD trajectories.

Figure 7 Calculated κ^3-weighted $\chi(\kappa)$ function (continuous lines) based on a 45:55 ratio of Cd-LEV and Cd-ERI obtained from (a) MD trajectories and (b) optimized structures from MD trajectories as described in section 2.5.

Figure 8 Two snapshots of the Cd-ERI structure from MD trajectories showing the Cd-coordination in the *eri* cavity. Cd^{2+} is either completely surrounded by H_2O (a) or partially linked to framework oxygen atoms (b).

Figures

Figure 1

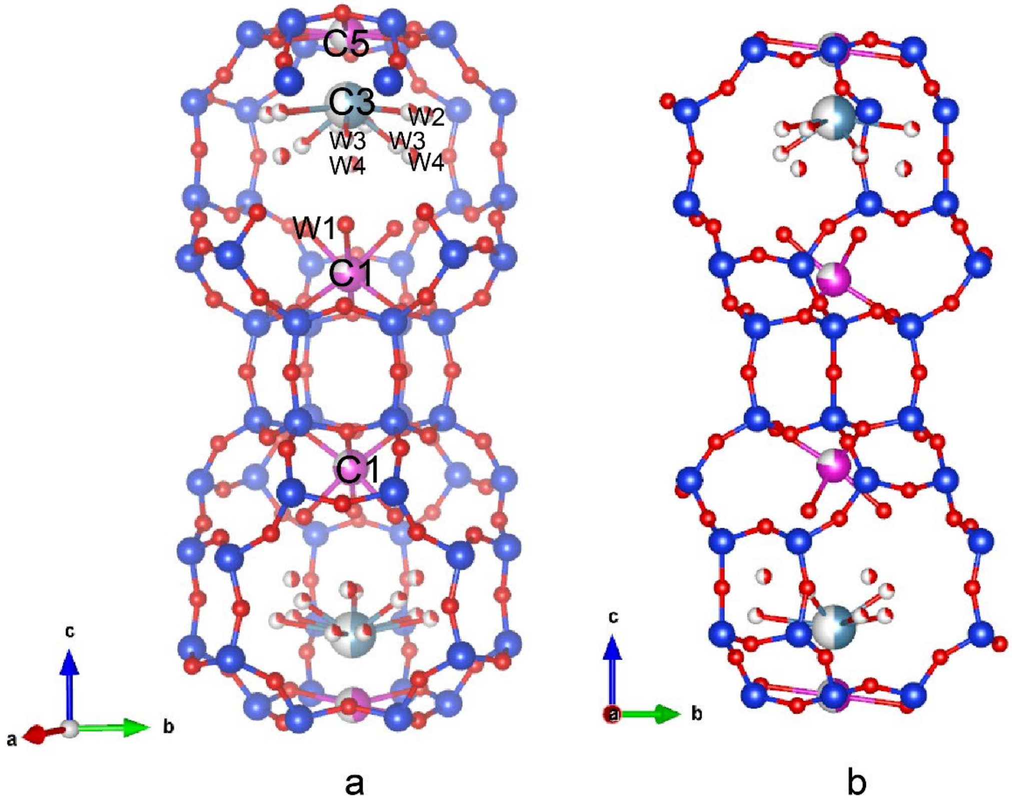

Figure 2

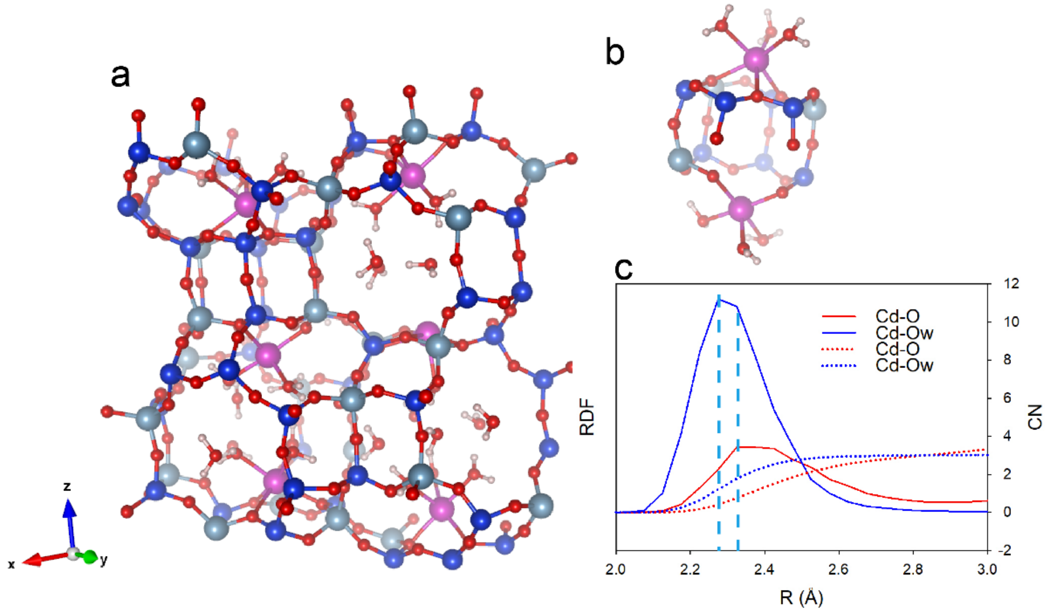

Figure 3

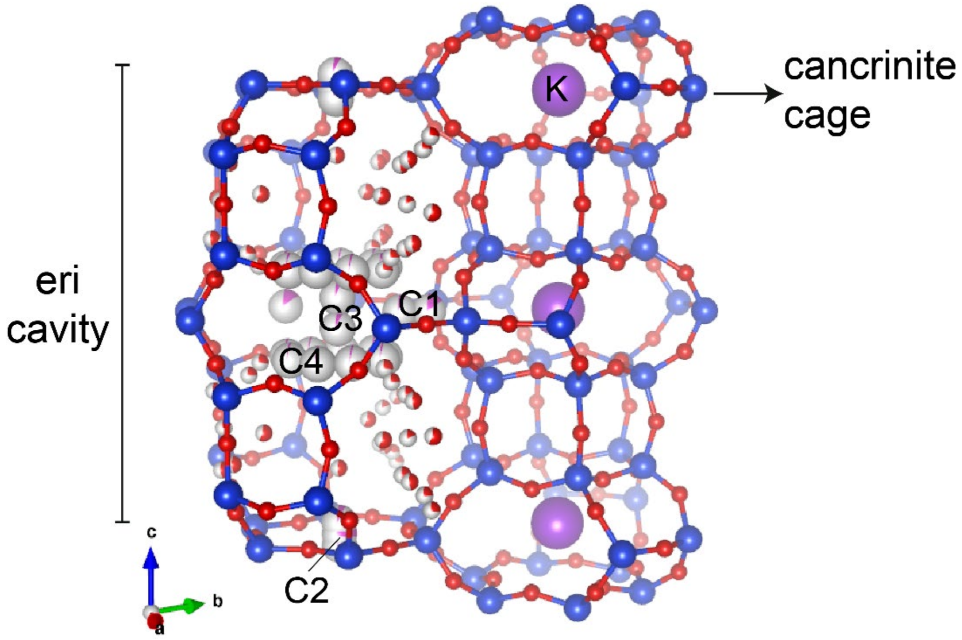

Figure 4

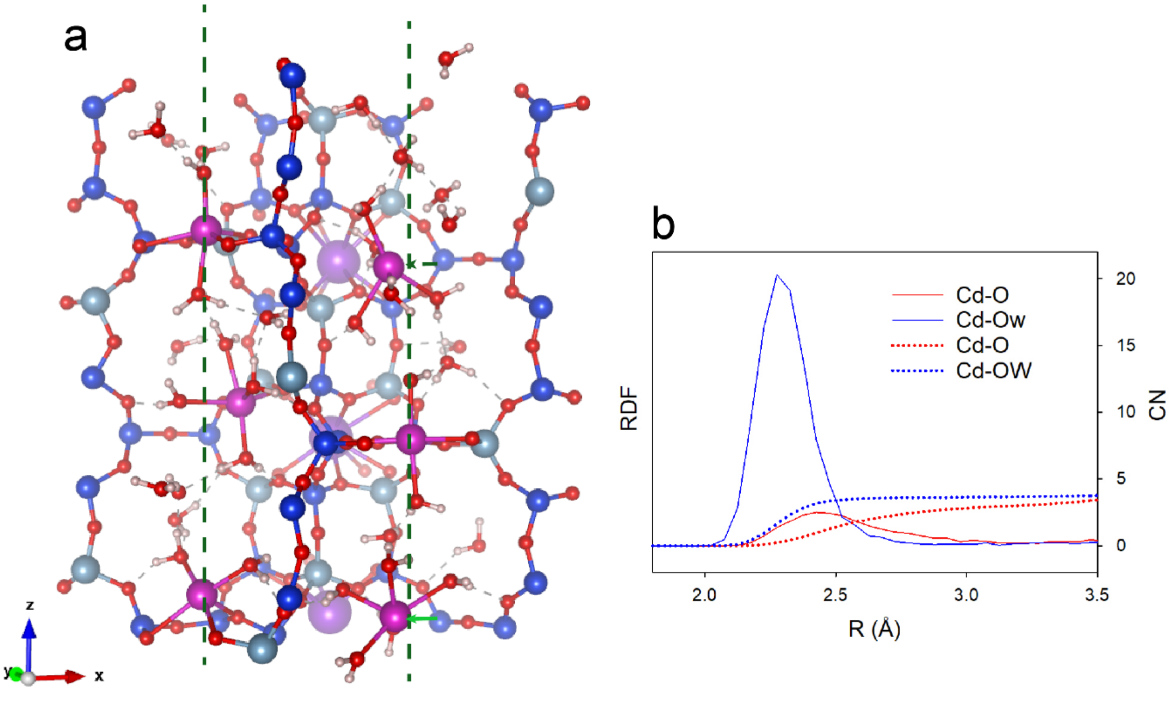

Figure 5

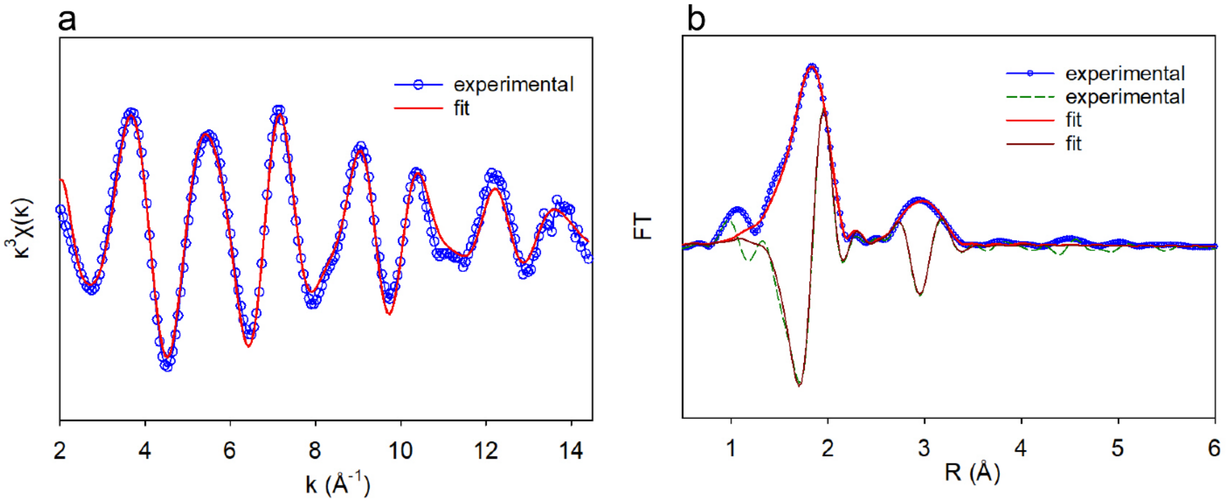

Figure 6

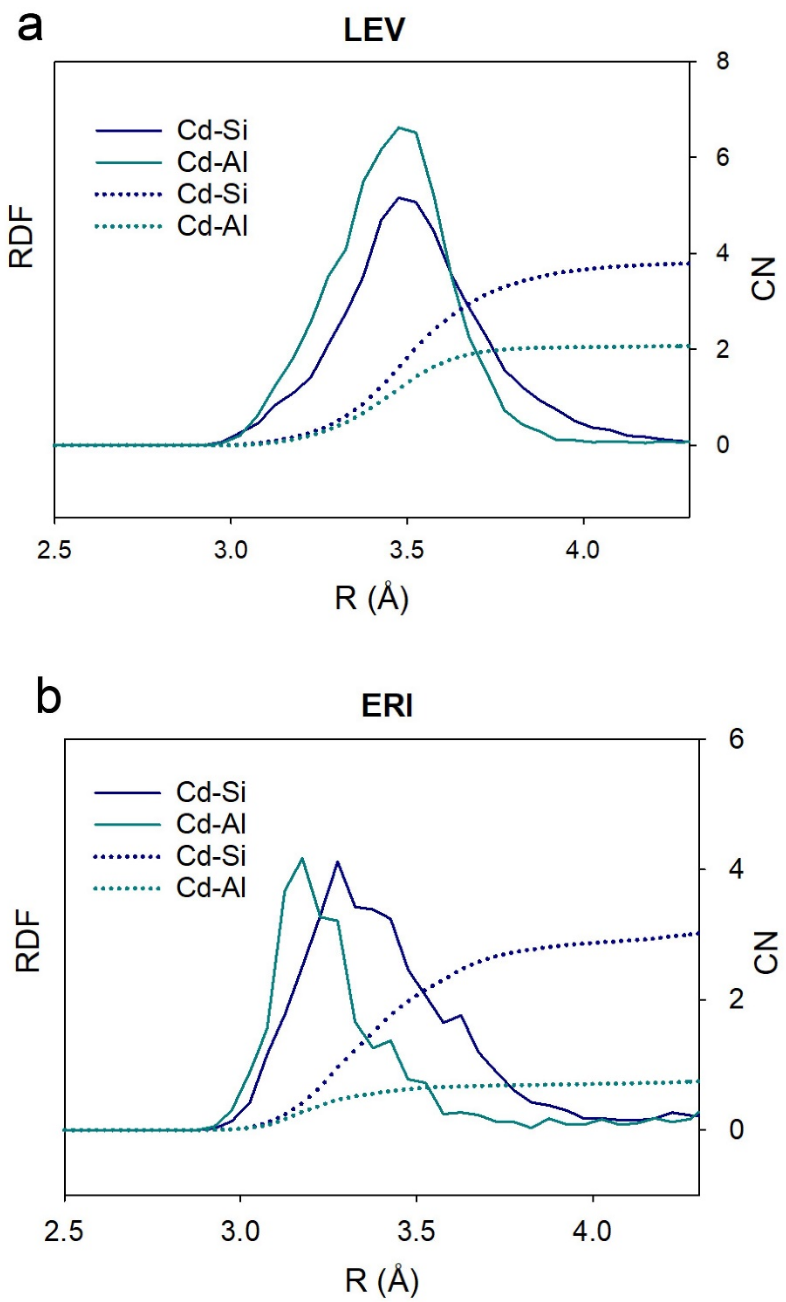
a
LEV
RDF
CN
Cd-Si
Cd-Al
Cd-Si
Cd-Al
8
6
4
2
0
2.5
3.0
3.5
4.0
R (Å)
b
ERI
RDF
CN
Cd-Si
Cd-Al
Cd-Si
Cd-Al
6
4
2
0
2.5
3.0
3.5
4.0
R (Å)

Figure 7

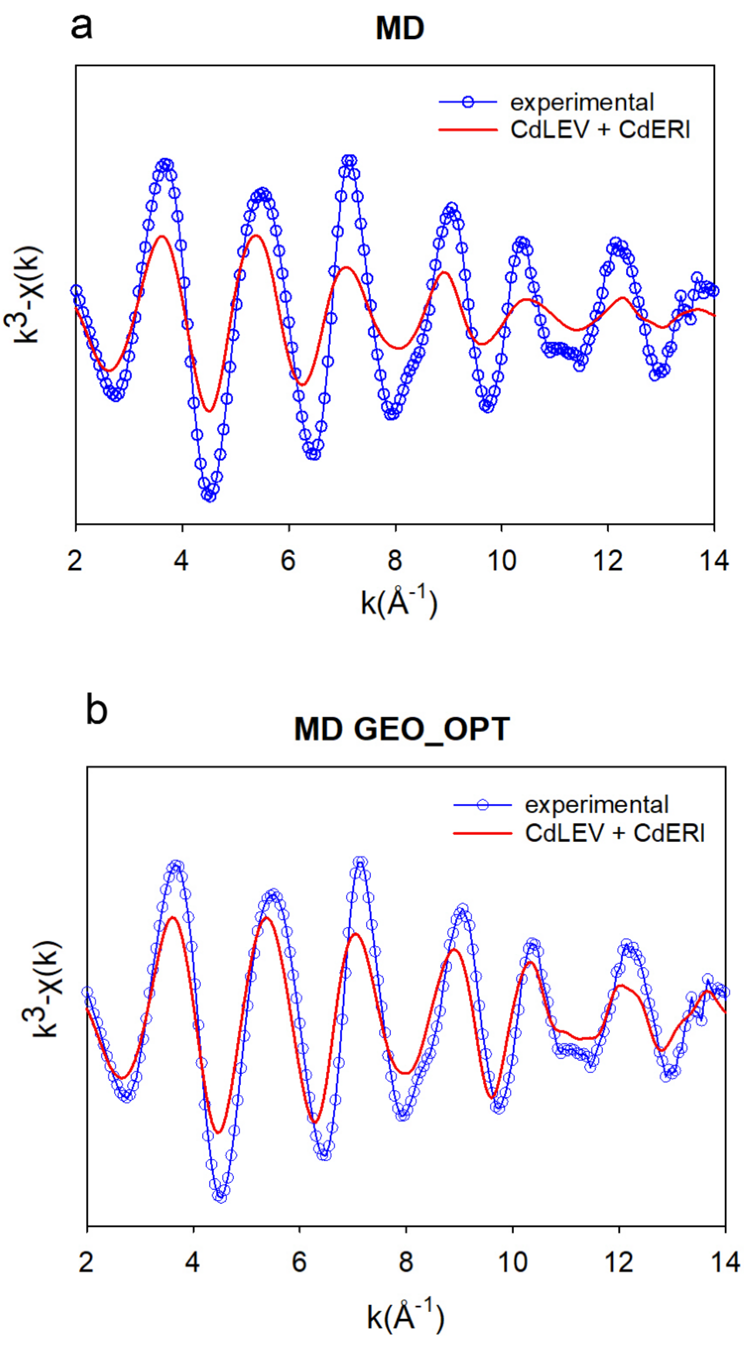
a
MD
experimental
CdLEV + CdERI
k^3-χ(k)
2
4
6
8
10
12
14
k(Å^{-1})
b
MD GEO_OPT
experimental
CdLEV + CdERI
k^3-χ(k)
2
4
6
8
10
12
14
k(Å^{-1})

Figure 8

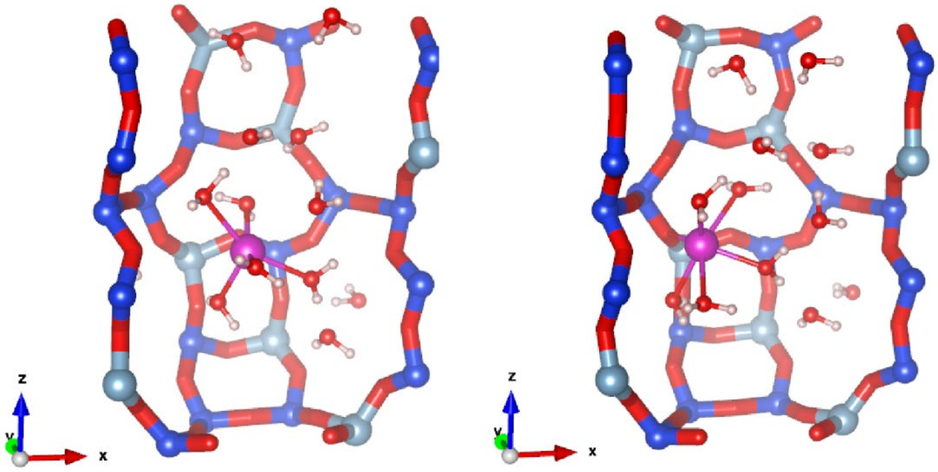

a

b